Quantum oscillatory exciton migration in photosynthetic reaction centers

Darius Abramavicius and Shaul Mukamel[a)]
Department of Chemistry, University of California, Irvine, 1102 Natural Sciences 2, Irvine, California 92697-2025, USA

(Received 22 April 2010; accepted 9 June 2010; published online 13 August 2010)

The harvesting of solar energy and its conversion to chemical energy is essential for all forms of life. The primary photon absorption, transport, and charge separation events, which trigger a chain of chemical reactions, take place in membrane-bound photosynthetic complexes. Whether quantum effects, stemming from entanglement of chromophores, persist in the energy transport at room temperature, despite the rapid decoherence effects caused by environment fluctuations, is under current active debate. If confirmed, these may explain the high efficiency of light harvesting and open up numerous applications to quantum computing and information processing. We present simulations of the photosynthetic reaction center of photosystem II that clearly establish oscillatory energy transport at room temperature originating from interference of quantum pathways. These signatures of quantum transport may be observed by two dimensional coherent optical spectroscopy. © *2010 American Institute of Physics*. [doi:10.1063/1.3458824]

I. INTRODUCTION

The capture of sunlight energy by photosynthetic complexes, its multistep transport, and trapping in reaction centers and the subsequent charge separation are the primary events in solar energy storage in plants and bacteria.[1–4] Wavelike energy transport lasting up to ~500 fs has been reported in two dimensional (2D) coherent electronic spectra of the Fenna–Matthews–Olson (FMO) complex at 77 K (Ref. 5) and more recently at room temperature.[6] It has been conjectured that these oscillations could originate from quantum transport, which is long lived due to the strong correlations of fluctuations of chromophore energies.[7] These quantum effects may increase the overall light harvesting efficiency through a delicate balance of coherent evolution and decoherence processes.[8–10] However, this conjecture is inconclusive since other sources of the observed oscillations could not be ruled out by these studies. These include macroscopic beating between the rephasing and nonrephasing contributions,[11,12] coherent molecular vibrations,[13] or non-Markovian relaxation memory effects of the bath.[14] Thus, spectral oscillations are not necessarily related to quantum properties of transport. One unambiguous signature of quantum transport is oscillatory population dynamics, which does not occur in classical transport, described by the Pauli master equation.

Energy relaxation and transport are usually described by coupling the exciton system to a phonon bath and deriving equations of motion for the reduced exciton density matrix ρ,

$$\dot{\rho}_{ab} = -\frac{i}{\hbar}[\hat{H}_S,\rho]_{ab} + \sum_{cd} K_{ab,cd}\rho_{cd}. \tag{1}$$

The first term represents the free exciton system, and the tetradic relaxation superoperator (RS) K represents dephasing and transport rates. Calculating K is a formidable computational challenge. Transport that takes place in the single-exciton, e, manifold requires $\sim N^4$ elements $K_{e_4e_3,e_2e_1}$ for an N chromophore aggregate. 2D signals further depend on the two-exciton manifold f which requires $\sim N^6$ elements. These can be calculated by using a model of weak coupling to a harmonic bath. The resulting Redfield RS is calculated to second order in the system-bath coupling and by further assuming a short bath correlation time (Markovian limit). A major drawback of this approach is that it only works in a limited parameter regime and otherwise yields an unphysical density matrix: populations may become negative or diverge.[15] To cure this problem an additional *secular approximation* is usually made: K is then reduced to a population block $K_{e_1e_1,e_2e_2}$, which describes a classical Pauli master equation for populations, and dephasing rates $K_{e_1e_2,e_1e_2}$ for the coherences. The remaining elements are set to zero. The secular RS guarantees to yield a physically acceptable density matrix in all parametric regimes. However, since the evolutions of populations and coherences are now decoupled, the transport is classical and shows no signatures of quantum coherences. We shall denote this level of theory as *classical transport* (CT).

An alternative approach is to evaluate the RS by starting with the Lindblad equations[16,17]

$$K\rho = \sum_\alpha \hat{V}_\alpha\rho\hat{V}_\alpha^\dagger - \frac{1}{2}\rho\hat{V}_\alpha^\dagger\hat{V}_\alpha - \frac{1}{2}\hat{V}_\alpha^\dagger\hat{V}_\alpha\rho. \tag{2}$$

Here $\hat{V}_\alpha$ is a set of system operators which represent the coupling of the exciton system to the environment. The Lindblad equations, well tested in quantum optics, guarantee a physically acceptable density matrix in all parametric regimes.[18] Moreover, since they are not limited to the secular approximation, they can couple populations and coherences. We shall denote the theory based on the Lindblad equations as *quantum transport* (QT). The main difficulty in their implementation is the lack of a microscopic procedure for

a)Electronic mail: smukamel@uci.edu.

finding $\hat{V}_\alpha$; the equations are derived using a stochastic model and are usually implemented phenomenologically.[18] This leaves a prohibitively large number of free parameters; in the singly excited e block there are $\sim N^2$ possible $\hat{V}_\alpha$ operators each containing $\sim N^2$ elements which give $\sim N^4$ undetermined parameters. When the f manifold is included this becomes $\sim N^6$.

In this paper we present a practical algorithm for constructing the entire Lindblad RS by using the following readily available ingredients as input: the Hamiltonian parameters of Eq. (3), the RS for the secular Redfield equations computed from a known bath spectral density, and the spatial overlaps of the modulus of the single-exciton wave functions. Using this algorithm, we demonstrate how quantum wavelike population transport translates into 2D spectroscopy signals. For a model of photosynthetic reaction center we predict that quantum transport originating from entanglement of chromophores and exciton relaxation pathways is possible and can be directly observed via diagonal peak oscillations of the photon echo (rephasing) 2D signal at room temperature despite the rapid decoherence.

II. THEORY

Electronic excitations of molecular aggregates are described by the Frenkel exciton Hamiltonian[4,19]

$$\hat{H}_S = \sum_m \varepsilon_m \hat{B}_m^\dagger \hat{B}_m + \sum_{mn}^{m\neq n} J_{mn} \hat{B}_m^\dagger \hat{B}_n, \tag{3}$$

where $\hat{B}_m(\hat{B}_m^\dagger)$ is the excitation annihilation (creation) operator at pigment m. ε_m is the excitation energy on pigment m and J_{mn} is the interpigment resonant interaction induced by Coulomb couplings. The exciton operator commutation relations

$$[\hat{B}_m, \hat{B}_n^\dagger] = \delta_{mn}(1 - 2\hat{B}_m^\dagger \hat{B}_m) \tag{4}$$

guarantee that two (or more) excitons may not reside on a given pigment. This is known as the hard-core boson model. In Ref. 19 we used the soft-core boson model where two excitations were allowed to reside on the same pigment; mathematically this amounts to using different commutation relations [Eq. (56) in Ref. 19]. The hard-core boson model is more suitable for electronic excitations of molecular complexes, while the soft-core model is preferable for weakly anharmonic vibrations.

Only the lowest three manifolds of eigenstates [Fig. 1(b)] are relevant for the 2D signals predicted here: the ground state $|g\rangle \equiv |0\rangle$, the single-excitons $|e\rangle = \Sigma_m \psi_{me} \hat{B}_m^\dagger |0\rangle$, and the double-excitons $|f\rangle = \Sigma_{mn}^{m>n} \Psi_{mn,f} \hat{B}_m^\dagger \hat{B}_n^\dagger |0\rangle$. The wave functions ψ and Ψ are obtained by diagonalizing Eq. (3).

To describe exciton dynamics we use Lindblad model (2) and further make the following single-body *ansatz* for the Lindblad operators:

$$\hat{V}_\alpha = \sum_{mn} u_{mn}^\alpha \hat{B}_m^\dagger \hat{B}_n, \tag{5}$$

where the matrix elements u_{mn}^α are complex numbers. The correlation matrix $C_{mn,m'n'} = \Sigma_\alpha u_{mn}^{\alpha *} u_{m'n'}^\alpha \equiv \langle u_{mn}^* u_{m'n'} \rangle$ contains the complete information required to construct the RS, as shown in Appendix A. C has $\sim N^4$, rather than $\sim N^6$, elements.

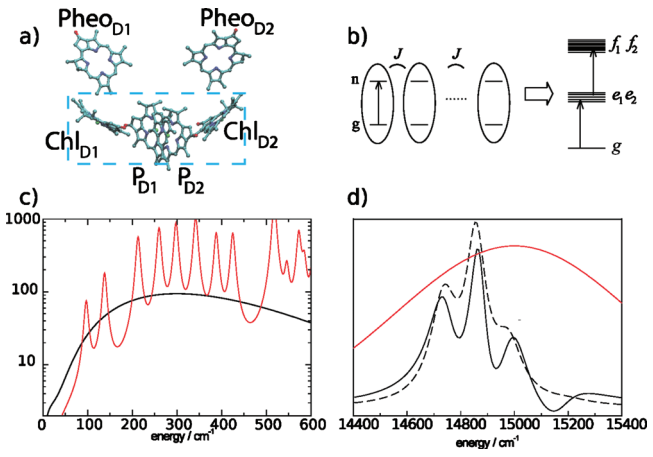

FIG. 1. (a) Pigment arrangement in the reaction center of photosystem II (RC of PS-II). The four closely packed pigments were used in the simulations. (b) The Frenkel exciton model representing local molecular excitations. The delocalized eigenstates are sketched on the right. The relevant eigenstates of RC of PS-II in our simulations are the ground state g with energy 0, four single-exciton states labeled e_1 to e_4 and six double-exciton states f_1 to f_6. All states are labeled in order of increasing energy. (c) Spectral density of molecular frequency fluctuations: (red) estimated from fluorescence line narrowing data (Refs. 20 and 21) and (black) spectral density used in the simulations. (d) Simulated absorption spectrum: (solid line) QT and (dashed line) CT. The red line denotes the 20 fs laser pulse power spectrum centered at 15 000 cm^{-1} used in the 2D simulations (Figs. 3–5).

The Lindblad operators in Eq. (5) contain a product of one creation and one annihilation operator. Thus acting by this operator on any state of the aggregate does not change the number of excitations. The Lindblad relaxation rates in Eq. (2) then conserve the number of excitons. Therefore the single- and double-exciton blocks are not mixed and the equations of motion are block-diagonal for the ground state, the single-exciton manifold and the double-exciton manifold. Had Lindblad operator in Eq. (5) included different numbers of creation and annihilation operators, the Lindblad relaxation would include interblock exciton transfer. We assume that such events are slow on our timescale and we do not consider them.

The Lindblad matrix can be related to exciton relaxation parameters known from Redfield relaxation theory. Consider the eigenstate basis, $C_{e_4e_3,e_2e_1} = \Sigma_{mnkl} C_{mn,kl} \psi_{me_4} \psi_{ne_3}^* \psi_{ke_2}^* \psi_{le_1}$. In the secular approximation, only autocorrelations are retained. Then $C_{ee',ee'} = K_{ee,e'e'}$ is the population relaxation rate from state e' to state e and $C_{ee,ee} = 2|K_{eg,eg}| - |K_{ee,ee}|$ is twice the pure dephasing of the eg coherence. These are known from a microscopic system-bath theory provided the spectral density is given.[22] The remaining elements of C go beyond the secular approximation and are unknown. However, they can be evaluated by making use of the scalar product property of C. The Schwartz inequality implies that

$$C_{e_4e_3,e_2e_1} = \sqrt{C_{e_4e_3,e_4e_3} C_{e_2e_1,e_2e_1}} \cos(\varphi_{e_4e_3,e_2e_1}). \tag{6}$$

The tetradic correlation angles satisfy $\cos(\varphi_{e_4e_3,e_2e_1}) = \cos(\varphi_{e_2e_1,e_4e_3})$ and $\cos(\varphi_{e_2e_1,e_2e_1}) = 1$.

TABLE I. Exciton model parameters (transition energies and excitonic interactions) of the central core of RC of PS-II (in cm^{-1}).

	P_{D1}	P_{D2}	Acc_{D1}	Acc_{D2}
P_{D1}	15 015	158	−29	−58
P_{D2}		15 015	−59	−27
Acc_{D1}			14 749	8
Acc_{D2}				14 992

We shall assume that the correlation cosine angles are directly related to the exciton spatial overlap factors $\xi_{ee'}=\Sigma_m|\psi_{me}||\psi_{me'}|$, which vary between 0 (no overlap) and 1 (complete overlap). We expect that only Lindblad operators involving overlapping excitons will be correlated. If the exciton overlaps vanish, their fluctuations should not be correlated and their Lindblad correlators must vanish. Three products of overlap factors are constructed in order to characterize the relation between excitons e_4, e_3, e_2, and e_1: $\xi_{e_4e_3}\cdot\xi_{e_2e_1}$, $\xi_{e_4e_2}\cdot\xi_{e_3e_1}$, and $\xi_{e_4e_1}\cdot\xi_{e_3e_2}$. We shall set $\cos(\varphi_{e_4e_3,e_2e_1})=1$ if the largest product is greater than a cutoff parameter $0<\eta<1$. Otherwise we set $\cos(\varphi_{e_4e_3,e_2e_1})=0$.

Using a single parameter η we can now construct full Lindblad correlation coefficient matrix and calculate the transport and relaxation parameters. This is described in Appendix A. Equation (B4) in Appendix B provides another constraint that guarantees that thermal equilibrium at long times coincides with $\rho_{ee'}\propto\delta_{ee'}\exp(-\beta\varepsilon_e)$; $\beta=(k_BT)^{-1}$. Based on the resulting relaxation operators, the simulated density matrix dynamics is nonsecular and contains QT. The resulting expressions for the optical signals are given in Appendix C.

This nonsecular exciton propagation theory can be extended to the nonlinear exciton equations (NEE).[23] For completeness the full set of relaxation operators for the NEE variables is presented in Appendix D. The NEE must then be solved numerically to calculate the optical signals in the quasiparticle representation.[19]

III. MODEL AND SIMULATION RESULTS

We applied our theory to the core of reaction center (RC) of photosystem II (PS-II), shown in Fig. 1(a).[24,25] The central part of the RC consists of two, D1 and D2, branches of pigments: the special pair, P_{D1} and P_{D2}, accessory Chl_{D1} and Chl_{D2}, and pheophytins, $Pheo_{D1}$ and $Pheo_{D2}$. These, together with two additional pigments, $Chlz_{D1}$ and $Chlz_{D2}$, form the primary exciton system.[26–28] Our simulations included the central four chlorophyll pigments, P_{D1}, P_{D2} and Acc_{D1}, Acc_{D2}, which are closely packed in the RC core. Pheo molecules were neglected to reduce numerical simulation cost.

The Hamiltonian parameters are known from previous simulations.[26–28] ε_m and J_{mn} elements of Eq. (3) were taken from Ref. 26 and are reported in Table I. The x-ray pigment structure is taken from Ref. 25 and the transition dipoles were assumed to pass through nitrogen b and d atoms. The single- and double-exciton eigenstates are obtained by diagonalizing the Hamiltonian. The calculated single- and double-exciton eigenstates with energies are given in Table II.

TABLE II. Single- and double-exciton eigenstate properties.

e state	Energy (cm^{-1})
1	14 736.4
2	14 856.6
3	14 978.3
4	15 199.7
f state	
1	29 600
2	29 715
3	29 850
4	29 911
5	30 036
6	30 201

The surrounding proteins cause decoherence through fluctuating transition energies of pigments. The homogeneous linewidth of chlorophyll complexes is typically ~60 cm^{-1}.[4] We model the spectral broadening by assuming that each chlorophyll frequency is coupled to a harmonic bath which induces uncorrelated energy fluctuations characterized by the spectral density

$$C''(\omega)=\lambda_L\frac{\omega}{\omega_L}e^{-|\omega|/\omega_L}+\lambda_H\left(\frac{\omega}{\omega_H}\right)^3e^{-|\omega|/\omega_H}. \quad (7)$$

We used $\omega_L=20$ cm^{-1} and $\omega_H=100$ cm^{-1} as the low and the high frequency fluctuating modes and λ_L and λ_H are the coupling strengths. Using this spectral density in the Markovian limit of Redfield theory, the first, λ_L, term is mostly responsible for the pure dephasing, and the second, λ_H, term induces population relaxation.[22] By setting $\lambda_H=70$ cm^{-1} and $\lambda_L=6.52$ cm^{-1} [the spectral density is shown in Fig. 1(c)] the secular rates $K_{eg,eg}$ and $K_{ee,e'e'}$ were computed using Eqs. (369) and (371) of Ref. 19; dephasing rate of the lowest-energy exciton state at 293 K ($K_{eg,eg}$) is 60 cm^{-1} (dephasing time of ~100 fs) and transport rates ($K_{ee,e'e'}$) are 10–50 cm^{-1} (100–500 fs time scale) in agreement with experiment.[20] The calculated single-exciton dephasing rates at temperature of 293 K, $K_{e_jg,e_jg}(j=1,2,3,4)$, are 60, 44.6, 62.6, and 92 cm^{-1}, respectively. The population transport rates, $K_{ee,e'e'}$, are given in Table III.

The rates $K_{ee,e'e'}$ and $K_{eg,eg}$ lead to the $C_{ee',ee'}$ matrix as described in Sec. II. The correlation cosines, $\cos(\varphi_{e_4e_3,e_2e_1})$, were computed using the exciton overlap cutoff $\eta=0.1$. The entire $C_{e_4e_3,e_2e_1}$ matrix was computed from Eq. (6) and then used to generate the nonsecular K elements for QT (see Appendix A). In CT, only the secular K elements were retained. For simplifying the analysis we further required the long

TABLE III. Single-exciton population rate matrix $K_{ee,e'e'}$ (in cm^{-1}).

e states	1	2	3	4
1	−5.5	7.6	2.1	5.9
2	4.2	−32	12	96
3	0.64	6.6	−24	30
4	0.61	18	9.9	−131

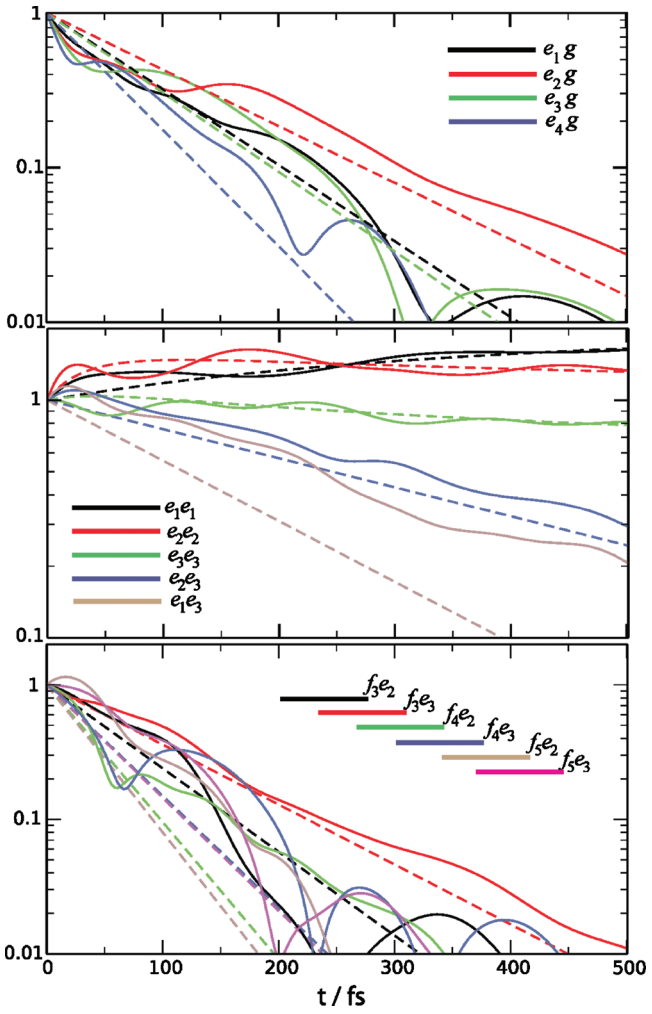

FIG. 2. Dynamics of selected density matrix elements in different exciton manifolds: (solid) QT and (dashed) CT. The amplitudes of selected density matrix elements $|\rho_{ab}|$ are shown as indicated. QT has oscillatory density matrix dynamics, while CT shows exponential decays of coherences and exponential equilibration for populations. The state labeling was defined in Fig. 1.

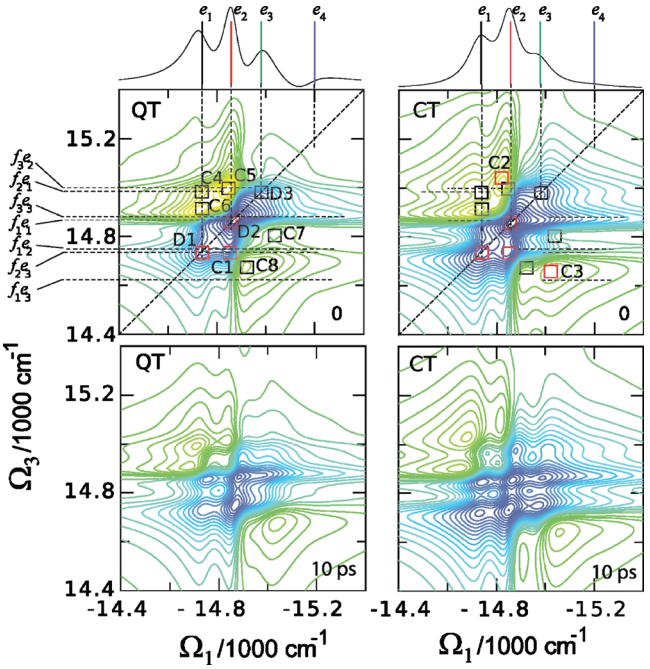

FIG. 3. Two dimensional photon echo signal at 0 and 10 ps t_2 delay times. The imaginary part of the full $S_{kl}^{(SOS)}(\Omega_3,t_2,\Omega_1)$ signal [Eqs. (42)–(44) in Ref. 19] is denoted $S(\Omega_3,t_2,\Omega_1)$. We normalized S to ten maximum value at $t_2=0$. In the figure we plot $\mathrm{arcsinh}(S)=\ln(S+\sqrt{1+S^2})$. This gives a logarithmic scale if $S>1$ and a linear scale if $S<1$, thus amplifying weak features in the spectrum and reducing large peaks: (left) QT, (right) CT; (top row) $t_2=0$, (bottom row) $t_2=10$ ps.

time (equilibrium) density matrix predicted by the QT RS to coincide with the canonical distribution of the isolated system as described in Appendix B; this puts additional constraints on C.

We next turn to the CT and QT exciton dynamics and their spectroscopic signatures. The QT expressions for optical signals are given in Appendix C: Green's functions were computed by numerical propagation of density matrix equations of motion with either secular or Lindblad relaxation rates. The simulated QT and CT exciton dynamics at room temperature in various exciton manifolds are shown in Fig. 2. In the CT, coherences decay exponentially, whereas QT shows modulations of the density matrix elements and the coherences survive for longer times (up to 500 fs). These reflect the entangled evolution of populations and coherences. The optical absorption spectrum, which only depends on the elements $\rho_{eg}(t)$, is shown in Fig. 1(d). In CT, the higher-energy peaks are broad due to their short lifetimes. These become narrower in the QT; the entangled dynamics equalizes the linewidths of all excitons.

We now turn to the 2D photon echo spectra;[19,29–31] four short laser pulses, separated by t_1, t_2, and t_3 delays, are used to detect the signal in the $\boldsymbol{k}_4=-\boldsymbol{k}_1+\boldsymbol{k}_2+\boldsymbol{k}_3$ direction. We used 20 fs Gaussian laser pulses centered at 15 000 cm^{-1} [see Fig. 1(d); laser spectral envelopes are $\mathcal{E}(\omega)\propto\exp(-\sigma^{-2}(\omega-\omega_0)^2)$ with $\sigma=884$ cm^{-1}]. The signal is represented in two dimensions using two dimensional one-sided Fourier transformations with respect to the time delays t_1 and t_3 (the conjugate frequency variables are Ω_1 and Ω_3). This yields rephasing photon echo 2D spectra. Transport occurs during t_2, which is varied as a parameter. The signal shows molecular correlations induced by static couplings and transport. The 2D signals depend on the following density matrix elements: $\rho^*_{eg}(t_1)$, $\rho_{ee'}(t_2)$, $\rho_{gg}(t_2)$, and $\rho_{eg}(t_3)$, $\rho_{fe}(t_3)$. The (Ω_3,Ω_1) QT and CT simulations for short ($t_2=0$) and at long (10 ps) delay, where the excited states are thermally equilibrated, are compared in Fig. 3. We mark the main QT peaks at $t_2=0$ by squares. The signal has two main diagonal peaks D1 and D2 (blue: negative) corresponding to the excitons e_1 and e_2, whose strength depends on their populations e_1e_1 and e_2e_2. The main crosspeak C1 is related to population transfer from e_2 to e_1. The weaker diagonal peak D3 represents the e_3 exciton. The other (yellow: positive) crosspeaks C4–C6 reflect double-exciton resonances. We indicate the related frequencies on the 2D plot: C4 is related to density matrix element f_2e_1, very strong peak C5 to f_3e_2, and C6 is shifted from f_1e_1 due to interference with blue peak similar to peaks C7 and C8. In CT we find that C4 and C7 vanish, and C5 and C8 shift toward C2 and C3, respectively. At $t_2=10$ ps delay, C1 becomes the strongest signifying exciton transfer. Note that a strong blue crosspeak between excitons e_3 and e_1 de-

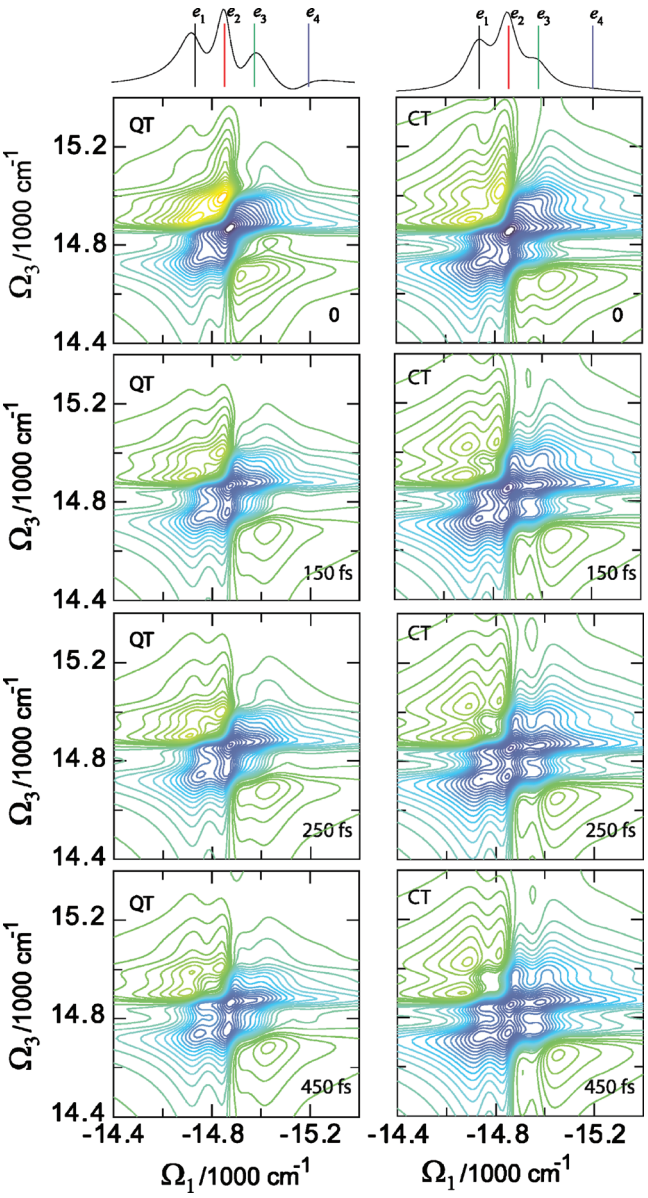

FIG. 4. Two dimensional photon echo signal at few t_2 delay times. The representation is the same as in Fig. 3; (left) QT and (right) CT.

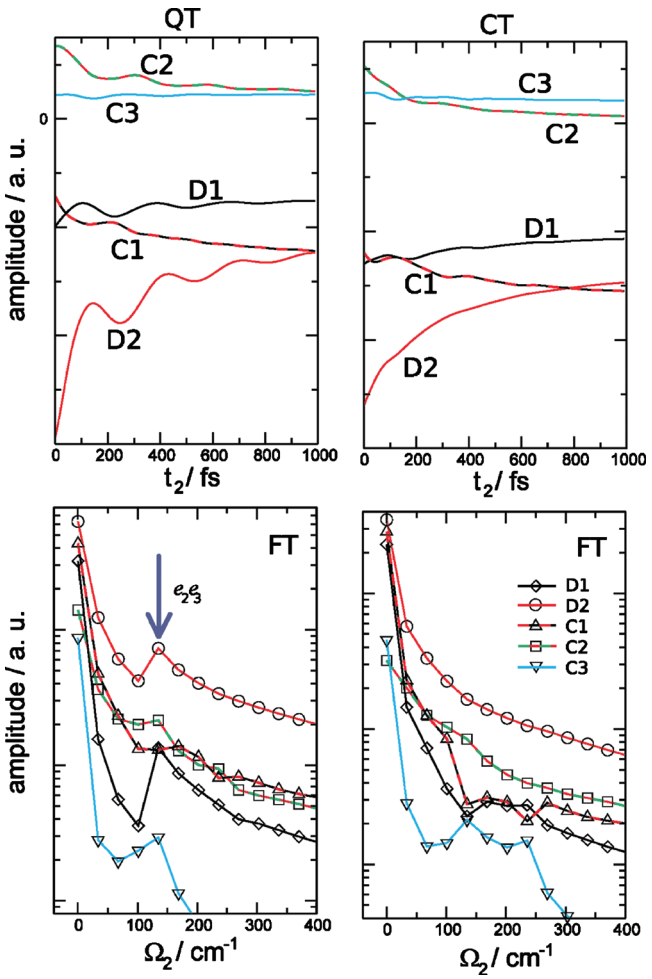

FIG. 5. Top: evolution of the unnormalized $S(\Omega_3,t_2,\Omega_1)$ signal at selected peaks D1 and D2 (diagonal) and C1, C2, and C3 (cross peaks) of Fig. 3. Bottom: Fourier transform of the curves given at the top. The peak is marked by an arrow: (left) QT and (right) CT.

velops in CT but is much weaker in QT. In CT the peak is associated with population transfer from e_3 to e_1. In QT the transfer occurs in an indirect pathway: coherences interfere so many more pathways and various resonant frequencies are involved. The overall spectral pattern of QT and CT is similar but details (some peaks, spectral linewidths, and peak amplitudes) are different. This is because for both of these delays the QT and CT t_2 evolutions are the same (no evolution at $t_2=0$, thermal equilibrium at $t_2=10$ ps). Thus the signals only differ by the ρ_{eg} and ρ_{fe} propagations during t_1 and t_3. In QT the peaks are narrower and therefore much higher, especially the yellow peaks above the diagonal line.

The QT and CT dynamics are markedly different in the t_2 time evolution of the diagonal peaks (D1 and D2) and crosspeaks (C1, C2, and C3), as depicted in Figs. 4 and 5 (yellow C5 and C8 areas strongly overlap with blue in CT). QT shows strong oscillations of D1 and D2 lasting for over 600 fs. These reflect the nonequilibrium populations (Fig. 2) and are correlated with the beating of C2 and C1. The entire high-resolution (each 10 fs) evolution of the 2D spectra between $t_2=0$ and 1 ps for CT and QT simulations (MPEG-4 FourCC of FMP4) movies) is presented in Ref. 32. The CT simulations also show rapidly decaying (~300 fs) oscillations of C1 and C2 (these are related to coherences showing quantum beats), the population peaks D1 and D2 are nonoscillatory. The absence of oscillations in diagonal peaks, thus, indicates CT. To help trace the origin of the QT oscillatory motion we also depict in Fig. 5 the Fourier transform of the peak evolutions. The 130 cm^{-1} peak of QT corresponds to the coherence ρ_{23} signifying the strong coupling between the populations ρ_{11}, ρ_{22}, and the coherence ρ_{23}. This coupling is missed by CT.

IV. DISCUSSION AND CONCLUSIONS

Our simulations demonstrate that the Lindblad theory may account for strong coupling of populations and coherences and clear signatures of QT in 2D rephasing signals can be observed even at room temperature. Figures 2 and 3 reveal that population relaxation acquires oscillatory components due to its coupling with coherence oscillations. The oscillation frequencies depend on the coupling strength and

may be different from the coherence oscillation frequencies.[15] The otherwise fast decaying density matrix components are fed by the slowly decaying nonequilibrium populations. The coherences survive for longer times. Oscillatory population dynamics translates into long-lived oscillations of the diagonal and off-diagonal peaks in the 2D spectra (Fig. 4). The corresponding diagonal peaks do not show oscillations in CT. Oscillatory diagonal peaks are thus a clear signature of QT. This conclusion holds only for the rephasing 2D signal calculated here. The quantum beats of the combined rephasing and nonrephasing signals or of off-diagonal peaks in Refs. 5 and 6 do not necessarily imply QT since nonrephasing 2D diagonal peaks include stimulated emission coherences which oscillate even in the CT case. QT can be distinguished from vibrational coherences[13] as well since the vibration-induced oscillations correlate with known vibrational frequencies. It is more difficult to rule out the QT and classical non-Markovian relaxation memory effects. Our simulations suggest that quantum transport may be an important factor in energy transport in other photosynthetic complexes[5] and strongly coupled molecular aggregates, such as linear and cylindrical J aggregates,[33] and may be unambiguously observed experimentally at room temperature. Chromophore entanglement survives the decoherence process.

The Lindblad equation is derived in the Markovian limit, so that the equation of motion is local in time, and slow bath-induced correlation effects are neglected. Environment fluctuations in pigment protein complexes may have very broad spectrum of fluctuations. These are induced by protein backbone, side chains, water molecules, and the intramolecular pigment vibrations. The Markovian model represents the fastest fluctuations, which are induced by e.g., water molecules and high-frequency protein backbone fluctuations. A full microscopic model is needed to include all fluctuations. A simplified model may be used by distinguishing the slow and fast bath degrees of freedom. All transport phenomena are induced by the fast degrees of freedom. These can be represented by Lindblad relaxation theory. The slow degrees of freedom may be included by static disorder. The slow bath-induced environment fluctuations in the secular approximation have been successfully included using cumulant-expansion techniques.[34] These should be extended to QT.

The presented model of the RC is crude and our results are qualitative. Comparison with the experiment will require to fine tune the parameters and include additional chromophores. The RC core part demonstrates that quantum transport in the RC is possible, and the QT signature is oscillatory t_2 dynamics of diagonal peaks in the 2D photon echo rephasing signal. Experimental evidence for the spectral dynamics predicted here will provide a clear signature for QT in photosynthetic complexes.

ACKNOWLEDGMENTS

The support of the National Science Foundation (Grant No. CHE0745892) is gratefully acknowledged. We wish to thank Dr. Marten Richter for useful discussions.

APPENDIX A: THE COMPLETE LINDBLAD RELAXATION SUPEROPERATORS

In the full space of eigenstates a, $b=g$, e, and f we write the Lindblad operator in a matrix form,

$$\hat{V}_\alpha = \sum_{ab} V_{ab}^{(\alpha)} |a\rangle\langle b|. \tag{A1}$$

Using Eq. (4), the $\hat{V}$ operators conserve the number of excitons and are block-diagonal. For elements involving the ground state, g, we get

$$V_{ga}^{(\alpha)} = V_{ag}^{(\alpha)} = 0, \quad a = g,e,f. \tag{A2}$$

For the single-exciton block we simply have

$$V_{ee'}^{(\alpha)} \equiv u_{ee'}^{(\alpha)}. \tag{A3}$$

To calculate matrix elements involving f we first use the unitary transformation

$$u_{mn} = \sum_{ee'} \psi_{me}\psi_{ne'}^* u_{ee'}. \tag{A4}$$

Product states of two local excitations $|mn\rangle = \hat{B}_m^\dagger \hat{B}_n^\dagger |0\rangle$ constitute a basis of double excitations. In this basis the matrix elements are

$$\langle mn|\hat{V}_\alpha|kl\rangle \equiv V_{(mn)(kl)}^{(\alpha)} = u_{mk}^{(\alpha)}\delta_{nl} + u_{nl}^{(\alpha)}\delta_{mk}, \tag{A5}$$

where $m>n$ and $k>l$. Transformation to the double-exciton eigenstates gives

$$V_{ff'}^{(\alpha)} = \sum_{mn}^{m>n} \sum_{kl}^{k>l} \Psi_{(mn)f}^* \Psi_{(kl)f'} V_{(mn)(kl)}^{(\alpha)}. \tag{A6}$$

All matrix elements of the Lindblad operators $\hat{V}$ in the ground state (g), single-exciton (e), and double-exciton (e) manifolds are now defined.

Using these results we find the following nonzero Lindblad correlation matrices

$$\langle V_{e_4e_3}^* V_{e_2e_1}\rangle \equiv C_{e_4e_3,e_2e_1}, \tag{A7}$$

$$\langle V_{e_4e_3}^* V_{f_2f_1}\rangle = \sum_{e_2e_1} C_{e_4e_3,e_2e_1} \sum_{mn}^{m>n} \sum_{kl}^{k>l} \Psi_{(mn)f_2}^* \Psi_{(kl)f_1} [\delta_{nl}\psi_{me_2}^*\psi_{ke_1} + \delta_{mk}\psi_{ne_2}^*\psi_{le_1}], \tag{A8}$$

and finally

$$\langle V^*_{f_4f_3}V_{f_2f_1}\rangle = \sum_{e_4e_3e_2e_1} C_{e_4e_3,e_2e_1} \sum_{m_1n_1}^{m_1>n_1} \sum_{k_1l_1}^{k_1>l_1} \sum_{mn}^{m>n} \sum_{kl}^{k>l} \Psi_{(m_1n_1)f_4}\Psi^*_{(k_1l_1)f_3}\Psi^*_{(mn)f_2}\Psi_{(kl)f_1}[\delta_{n_1l_1}\delta_{nl}\psi_{m_1e_4}\psi^*_{k_1e_3}\psi^*_{me_2}\psi_{ke_1}$$
$$+ \delta_{m_1k_1}\delta_{nl}\psi_{n_1e_4}\psi^*_{l_1e_3}\psi^*_{me_2}\psi_{ke_1} + \delta_{n_1l_1}\delta_{mk}\psi_{m_1e_4}\psi^*_{k_1e_3}\psi^*_{ne_2}\psi_{le_1} + \delta_{m_1k_1}\delta_{mk}\psi_{n_1e_4}\psi^*_{l_1e_3}\psi^*_{ne_2}\psi_{le_1}]. \quad \text{(A9)}$$

We now turn to the RS. Because of our form of the Lindblad operator, the density matrix dynamics splits into four separate blocks. These are the coherences between single-excitons and the ground state ρ_{eg}, the full single-exciton block $\rho_{ee'}$, the coherences between the double-exciton and the ground state ρ_{fg} (this is not needed for the signals calculated here) and the double- and single-exciton blocks ρ_{fe}.

For ρ_{eg} we have

$$K_{eg,e'g} = -\frac{1}{2}\sum_{e_1} C_{e_1e,e_1e'}. \quad \text{(A10)}$$

This represents the coherence transfer ($e \neq e'$) and exciton dephasing ($e=e'$) rates.

For the $\rho_{ee'}$ block we have a nonsecular transport matrix, which couples population and coherence dynamics

$$K_{e_1e_2,e'_1e'_2} = C_{e_2e'_2,e_1e'_1} + \delta_{e_1e'_1}K_{e'_2g,e_2g} + \delta_{e_2e'_2}K_{e_1g,e'_1g}. \quad \text{(A11)}$$

For the ρ_{fg} block we get

$$K_{fg,f'g} = -\frac{1}{2}\sum_{f_1} \langle V^*_{f_1f}V_{f_1f'}\rangle. \quad \text{(A12)}$$

Finally for ρ_{fe} we have

$$K_{(f_1e_1),(f_2e_2)} = \langle V^*_{e_1e_2}V_{f_1f_2}\rangle + \delta_{e_1e_2}K_{f_1g,f_2g} + \delta_{f_1f_2}K_{e_2g,e_1g}. \quad \text{(A13)}$$

The correlations $\langle V^*_{f_1f}V_{f_1f}\rangle$ and $\langle V^*_{e_1e_2}V_{f_1f_2}\rangle$ are given in terms of C by Eqs. (A8) and (A9). This completes the set of relaxation superoperators in our relevant space of states required for computing third order signals.

APPENDIX B: CONSTRAINS FOR THE LINDBLAD RELAXATION SUPEROPERATOR

To simplify the analysis we require the Lindblad equation to yield at long times the canonical equilibrium distribution of the isolated system $\rho^{(\infty)}=\exp(-\beta\hat{H}_S)$, where $\beta=(k_BT)^{-1}$. The equilibrium exciton populations are then given by $\rho^{(\infty)}_{ee}\propto\exp(-\beta\varepsilon_e)$, where ε_e is energy of exciton state e, and all off-diagonal coherences vanish: $\rho^{(\infty)}_{ee'}=0$ for $e\neq e'$.

For the equilibrated state the Lindblad equation for all e_1 and e_2 gives

$$0 = \sum_{e'}\Bigg[C_{e_2e',e_1e'} - \frac{1}{2}\sum_{e''}(\delta_{e_1e'}C_{e''e',e''e_2} + \delta_{e_2e'}C_{e''e_1,e''e'})\Bigg]\exp(-\beta\varepsilon_{e'}). \quad \text{(B1)}$$

We first note that this equation is satisfied when the Lindblad operator matrix elements are completely uncorrelated, i.e., $C_{e_1e_2,e'e''}=\delta_{e_1e'}\delta_{e_2e''}C_{e_1e_2,e_1e_2}$.[15] This leads to the secular relaxation RS,

$$K^{(S)}_{e_1e_2,e'_1e'_2} = [\delta_{e_1e_2}\delta_{e'_1e'_2} + (1-\delta_{e_1e_2})\delta_{e_1e'_1}\delta_{e_2e'_2}]K_{e_1e_2,e'_1e'_2}. \quad \text{(B2)}$$

This satisfies detailed balance and our requirement is met.

A more interesting case where our requirement holds is derived by recasting Eq. (B1) in the form

$$0 = \sum_{e_3}\Bigg[C_{e_2e_3,e_1e_3}\exp(-\beta\varepsilon_{e_3}) - \frac{1}{2}C_{e_3e_1,e_3e_2}\exp(-\beta\varepsilon_{e_1}) - \frac{1}{2}C_{e_3e_1,e_3e_2}\exp(-\beta\varepsilon_{e_2})\Bigg]. \quad \text{(B3)}$$

A sufficient condition for Eq. (B1) is

$$\frac{C_{e_1e_2,e_3e_4}}{\exp(-\beta\varepsilon_{e_3})+\exp(-\beta\varepsilon_{e_1})} = \frac{C_{e_4e_3,e_2e_1}}{\exp(-\beta\varepsilon_{e_2})+\exp(-\beta\varepsilon_{e_4})}. \quad \text{(B4)}$$

It is obtained by requiring that each term in the summation over e_3 in Eq. (B3) vanishes.

Only half-triangle of the $C_{e_4e_3,e_2e_1}$ matrix (for indices $e_1>e_2$, when $e_4=e_3$ and for all e_1 and e_2 when $e_4<e_3$) now must be calculated using the exciton overlaps as described in Sec. II. The other half can be obtained using Eq. (B4).

APPENDIX C: OPTICAL SIGNALS WITH QUANTUM TRANSPORT

The absorption spectrum is obtained by extending Eq. 268 of Ref. 19 to include QT (i.e., nonsecular propagation),

$$A(\omega) = \Im\sum_{e_2e_1}\langle\mu_{e_2g}\mu_{e_1g}\rangle\int_0^\infty \omega\, d\tau \exp(i\omega\tau)G_{e_2e_1}(\tau), \quad \text{(C1)}$$

where μ_{e_2g} is the transition dipole between the exciton state $|e_2\rangle$ and the ground state, and $G_{e_2e_1}(\tau)$ is Green's function describing single-exciton coherence ρ_{eg} propagation from ρ_{e_1g} at $t=0$ to ρ_{e_2g} at $t=\tau$.

By direct extension of Eqs. (13) and (42)–(44) of Ref. 19 we can write the following expressions for the *ground state bleach* (GSB), *excited state emission* (ESE), and *excited state absorption* (ESA) contributions to the photon echo 2D signal. The 2D photon echo ($\mathbf{k}_I$) signal is given by the sum of these three components:

$$S_{k_I,\mathrm{GSB}}(\Omega_3,t_2,\Omega_1)=\left(\frac{i}{\hbar}\right)^3\sum_{e_4e_3e_2e_1}\langle\mu_{e_4g}^{\nu_4}\mu_{e_3g}^{\nu_3}\mu_{e_2g}^{\nu_2}\mu_{e_1g}^{\nu_1}\rangle\mathcal{E}(\omega_4-\varepsilon_{e_4})\mathcal{E}(\omega_3-\varepsilon_{e_3})$$
$$\times\mathcal{E}(\omega_2-\varepsilon_{e_2})\mathcal{E}(\omega_1-\varepsilon_{e_1})G_{e_4e_3}(\Omega_3)\theta(t_2)G^*_{e_2e_1}(-\Omega_1), \tag{C2}$$

$$S_{k_I,\mathrm{ESE}}(\Omega_3,t_2,\Omega_1)=\left(\frac{i}{\hbar}\right)^3\sum_{e_4e_3e_2e_1}\langle\mu_{e_4g}^{\nu_4}\mu_{e_3g}^{\nu_3}\mu_{e_2g}^{\nu_2}\mu_{e_1g}^{\nu_1}\rangle\mathcal{E}(\omega_4-\varepsilon_{e_4})\mathcal{E}(\omega_3-\varepsilon_{e_3})\mathcal{E}(\omega_2-\varepsilon_{e_2})\mathcal{E}(\omega_1-\varepsilon_{e_1})$$
$$\times\sum_{e_2'e_1'}G_{e_4e_2'}(\Omega_3)\mathcal{G}^{(N)}_{e_2'e_3,e_2e_1'}(t_2)G^*_{e_1'e_1}(-\Omega_1), \tag{C3}$$

$$S_{k_I,\mathrm{ESA}}(\Omega_3,t_2,\Omega_1)=-\left(\frac{i}{\hbar}\right)^3\sum_{f_2f_1}\sum_{e_4e_3e_2e_1}\langle\mu_{f_2e_4}^{\nu_4}\mu_{f_1e_3}^{\nu_3}\mu_{e_2g}^{\nu_2}\mu_{e_1g}^{\nu_1}\rangle\mathcal{E}(\omega_4-\varepsilon_{f_2}+\varepsilon_{e_4})\mathcal{E}(\omega_3-\varepsilon_{f_1}+\varepsilon_{e_3})\mathcal{E}(\omega_2-\varepsilon_{e_2})$$
$$\times\mathcal{E}(\omega_1-\varepsilon_{e_1})\sum_{e_2'e_1'}\mathcal{G}^{(Z)}_{f_2e_4,f_1e_2'}(\Omega_3)\mathcal{G}^{(N)}_{e_3e_2',e_2e_1'}(t_2)G^*_{e_1'e_1}(-\Omega_1). \tag{C4}$$

$\mathcal{G}^{(N)}_{e_4e_3,e_2e_1}(t)$ is Green's function for single-exciton density matrix $\rho_{ee'}$ which represents the propagation amplitude from $\rho_{e_2e_1}$ to $\rho_{e_4e_3}$ and $\mathcal{G}^{(Z)}_{f_2e_2,f_1e_1}(t)$ is the corresponding Green's function for ρ_{fe}. These Green's functions simplify in the secular approximation since then $G_{ee'}\propto\delta_{ee'}$, $\mathcal{G}^{(N)}_{e_4e_3,e_2e_1}\propto\delta_{e_4e_2}\delta_{e_3e_1}$ (dephasing) or $\delta_{e_4e_3}\delta_{e_2e_1}$ (transport), and $\mathcal{G}^{(Z)}_{f_2e_2,f_1e_1}\propto\delta_{f_2f_1}\delta_{e_2e_1}$ and we recover expressions (42)–(44) of Ref. 19.

APPENDIX D: RELAXATION PARAMETERS IN THE NONLINEAR EXCITON EQUATIONS

The NEEs provide an alternative approach for calculating the nonlinear optical signals of excitons based on a quasiparticle representation rather than the sum over eigenstates used in this letter. That approach scales more favorably with size, N, and is required for larger complexes.[19] For completeness we give here RS for the NEE.

The NEE are equations of motion for the following variables $\mathcal{B}=\langle\hat{B}\rangle$, $\mathcal{N}=\langle\hat{B}^\dagger\hat{B}\rangle$, $\mathcal{Y}=\langle\hat{B}\hat{B}\rangle$, and $\mathcal{Z}=\langle\hat{B}^\dagger\hat{B}\hat{B}\rangle$. They are defined in the real space basis of molecular excitations ($|m\rangle=\hat{B}_m^\dagger|0\rangle$, $|mn\rangle=\hat{B}_m^\dagger\hat{B}_n^\dagger|0\rangle$).

In order to use the QT relaxation operators in the NEE we establish the relationship between the NEE variables and the density matrix elements. The NEE variables are calculated as expectation values in the Heisenberg representation. For the $\mathcal{B}$ variables we have

$$\mathcal{B}_m(t)\equiv\mathrm{Tr}\{e^{i\hat{H}_St}\hat{B}_me^{-i\hat{H}_St}\rho_0\}=\mathrm{Tr}\{\hat{B}_m\rho_t\}=\rho_{mg}(t). \tag{D1}$$

For the $\mathcal{N}$ variable we find $\mathcal{N}_{mn}\equiv\langle\hat{B}_m^\dagger\hat{B}_n\rangle^{(2)}=\rho_{nm}$. We rationalize this by noting that single-exciton $\mathcal{B}$ and $\mathcal{N}$ variables evolve only within the single-exciton manifold in the third order response. The $\mathcal{Y}_{mn}=\langle\hat{B}_m\hat{B}_n\rangle$ variables represent the double-exciton states. Note that the density matrix is defined in the complete orthogonal basis. This is guaranteed by taking $m\geq n$ for double-excitons. $\mathcal{Y}_{mn}$ is not restricted by that. We find that $\mathcal{Y}_{mn}(t)\equiv\rho_{(mn)g}(t)$, where for the density matrix we keep only $m\geq n$, while $\mathcal{Y}_{mn}=\mathcal{Y}_{nm}$. This difference can be accounted for by comparing the equations of motion. The NEE three-operator variable $\mathcal{Z}_{kmn}=\langle\hat{B}_k^\dagger\hat{B}_m\hat{B}_n\rangle$ is the three-particle variable. In this space we find that $\mathcal{Z}_{kmn}(t)\equiv\langle[\hat{B}_k^\dagger\hat{B}_m\hat{B}_n]_t\rangle=\mathrm{Tr}\{\hat{B}_m\hat{B}_n\rho_t\hat{B}_k^\dagger\}$, which gives the density matrix element $\mathcal{Z}_{kmn}(t)=\rho_{(mn)k}(t)$ with $m\geq n$ and $\mathcal{Z}_{kmn}(t)=\mathcal{Z}_{knm}(t)$.

This establishes the connection between the density matrix elements and the NEE variables. Having the Lindblad equation for the density matrix we can now write the Lindblad-type relaxation operators for the NEE variables.

We first switch to the single-exciton product basis by $\hat{B}_e=\Sigma_m\psi_{em}\hat{B}_m$ with the inverse $\hat{B}_m=\Sigma_e\psi_{em}^*\hat{B}_e$. We can now transform the system Hamiltonian, the commutation relations, and the system-field interaction into the single-exciton eigenstate basis and we get the new set of NEE variables $\mathcal{B}_e$, $\mathcal{N}_{ee'}$, $\mathcal{Y}_{ee'}$, and $\mathcal{Z}_{e_1ee'}$. $\mathcal{B}_e$ and $\mathcal{N}_{ee'}$ are "diagonal" variables, i.e., their homogeneous part of dynamical equation is diagonal since $\mathcal{B}$ and $\mathcal{N}$ are restricted to the single-exciton manifold. However the $\mathcal{Y}$ and $\mathcal{Z}$ variables are "nondiagonal" since the double-exciton eigenstates are not given by simple products of single-excitons. In this basis set the NEEs read[19]

$$\dot{\mathcal{B}}_e=-i\varepsilon_e\mathcal{B}_e+\sum_{e'}K^{(B)}_{ee'}\mathcal{B}_{e'}-i\sum_{e_1e_2e_3}V_{ee_1e_2e_3}\mathcal{Z}_{e_1e_2e_3}$$
$$+\mathcal{E}^{(\mathcal{B})}(t), \tag{D2}$$

$$\dot{\mathcal{N}}_{ee'}=-i\omega_{e'e}\mathcal{N}_{ee'}+\sum_{e_1e_2}K^{(\mathcal{N})}_{ee',e_1e_2}\mathcal{N}_{e_1e_2}+\mathcal{E}^{(\mathcal{N})}(t), \tag{D3}$$

$$\dot{\mathcal{Y}}_{ee'}=-i\sum_{e_1e_2}h^{(\mathcal{Y})}_{ee',e_1e_2}\mathcal{Y}_{e_1e_2}+\sum_{e_1e_2}K^{(\mathcal{Y})}_{ee',e_1e_2}\mathcal{Y}_{e_1e_2}+\mathcal{E}^{(\mathcal{Y})}(t), \tag{D4}$$

$$\dot{\mathcal{Z}}_{ee_1e_2} = -i\sum_{e_1'e_2'} h^{(\mathcal{Y})}_{ee',e_1'e_2'}\mathcal{Z}_{ee_1'e_2'} + i\varepsilon_e\mathcal{Z}_{ee_1e_2} + \sum_{e'e_1'e_2'} K^{(\mathcal{Z})}_{ee_1e_2,e'e_1'e_2'}\mathcal{Z}_{e'e_1'e_2'} + \mathcal{E}^{(\mathcal{Z})}(t), \tag{D5}$$

where V and $h^{(\mathcal{Y})}$ are tetradic matrices involving exciton couplings J. They are related to the exciton scattering, induced by Pauli exclusion [Eq. (4)]. $\mathcal{E}^{(\ldots)}(t)$ are terms related to interaction with the optical fields, and $K^{(\ldots)}$ are relaxation and transport matrices. For $\mathcal{Y}_{e_1e_2}$ and $\mathcal{Z}_{ee_1e_2}$ we allow any ordering of e_1 and e_2.

The relaxation operators for the NEE variables are obtained by comparing the NEE variables to the equations of the density matrix. The relaxation operator for $\mathcal{B}$ is the same as for the ρ_{eg} coherence,

$$K^{(\mathcal{B})}_{ee'} = K_{eg,e'g}. \tag{D6}$$

For the $\mathcal{N}$ variables we similarly get

$$K^{(\mathcal{N})}_{e_2e_1,e_2'e_1'} = K_{e_1e_2,e_1'e_2'}. \tag{D7}$$

For the $\mathcal{Y}$ variables we consider the Lindblad equation for ρ_{fg} density matrix element transformed into the basis of single-exciton products. Since $\mathcal{Y}_{ee'} \equiv \mathcal{Y}_{e'e}$, the relaxation operator $K^{(\mathcal{Y})}_{e_1e_2,e_1'e_2'}$ is defined for all combinations of indices. We then get

$$K^{(\mathcal{Y})}_{e_1e_2,e_1'e_1'} = \frac{\delta_{e_1'e_2'}+1}{2}\sum_{mn}\sum_{kl}\sum_{ff'}\psi_{me_1}\psi_{ne_2}\psi_{ke_1'}\psi_{le_2'} \times \Psi_{(mn)f}\Psi_{(kl)f'}K_{fg,f'g}, \tag{D8}$$

where we assume $\Psi_{(mn)f}=\Psi_{(nm)f}$ and $\Psi_{(mm)f}=0$. For the $\mathcal{Z}$ variables we similarly get

$$K^{(\mathcal{Z})}_{ee_1e_2,e'e_1'e_2'} = \frac{\delta_{e_1'e_2'}+1}{2}\sum_{mn}\sum_{kl}\sum_{ff'}\psi_{me_1}\psi_{ne_2}\psi_{ke_1'}\psi_{le_2'} \times \Psi_{(mn)f}\Psi_{(kl)f'}K_{fe',f'e}. \tag{D9}$$

[1] R. E. Blankenship, *Molecular Mechanisms of Photosynthesis* (Wiley-Blackwell, New York, 2002).
[2] G. R. Fleming and R. van Grondelle, Curr. Opin. Struct. Biol. **7**, 738 (1997).
[3] X. Hu, T. Ritz, A. Damjanovic, F. Autenrieth, and K. Schulten, Q. Rev. Biophys. **35**, 1 (2002).
[4] H. van Amerongen, L. Valkunas, and R. van Grondelle, *Photosynthetic Excitons* (World Scientific, Singapore, 2000).
[5] G. S. Engel, T. R. Calhoun, E. L. Read, T. K. Ahn, T. Mančal, Y. C. Cheng, R. E. Blankenship, and G. R. Fleming, Nature (London) **446**, 782 (2007).
[6] G. Panitchayangkoon, D. Hayes, K. A. Fransted, J. R. Caram, E. Harel, J. Wen, R. E. Blankenship, and G. S. Engel, "Long-lived quantum coherence in photosynthetic complexes at physiological temperature," e-print arXiv:1001.5108, 2010.
[7] E. Collini and G. D. Scholes, Science **323**, 369 (2009).
[8] M. Mohseni, P. Rebentrost, S. Lloyd, and A. Aspuru-Guzik, J. Chem. Phys. **129**, 174106 (2008).
[9] F. Caruso, A. W. Chin, A. Datta, S. F. Huelga, and M. Plenio, J. Chem. Phys. **131**, 105106 (2009).
[10] P. Rebentrost, M. Mohseni, and A. A. Guzik, J. Phys. Chem. B **113**, 9942 (2009).
[11] T. R. Calhoun, N. S. Ginsberg, G. S. Schlau-Cohen, Y.-C. Cheng, M. Ballottari, R. Bassi, and G. R. Fleming, J. Phys. Chem. B **113**, 16291 (2009).
[12] N. S. Ginsberg, I. C. Cheng, and G. R. Fleming, Acc. Chem. Res. **42**, 1352 (2009).
[13] D. Egorova, Chem. Phys. **347**, 166 (2008).
[14] L. Chen, R. Zheng, Q. Shi, and Y. Yan, J. Chem. Phys. **132**, 024505 (2010).
[15] B. Palmieri, D. Abramavicius, and S. Mukamel, J. Chem. Phys. **130**, 204512 (2009).
[16] D. A. Lidar, Z. Bihary, and K. B. Whaley, Chem. Phys. **268**, 35 (2001).
[17] *Irreversible Quantum Dynamics*, edited by F. Benatti and R. Floreanini (Springer, New York, 2003).
[18] N. G. van Kampen, *Stochastic Processes in Physics and Chemistry*, 3rd ed. (Elsevier, North Holland, 2007).
[19] D. Abramavicius, B. Palmieri, D. V. Voronine, F. Šanda, and S. Mukamel, Chem. Rev. (Washington, D.C.) **109**, 2350 (2009).
[20] V. I. Novoderezhkin, E. G. Andrizhiyevskaya, J. P. Dekker, and R. van Grondelle, Biophys. J. **89**, 1464 (2005).
[21] E. J. G. Peterman, H. van Amerongen, R. van Grondelle, and J. P. Dekker, Proc. Natl. Acad. Sci. U.S.A. **95**, 6128 (1998).
[22] V. Chernyak, T. Minami, and S. Mukamel, J. Phys. Chem. **112**, 7953 (2000).
[23] V. Chernyak, W. M. Zhang, and S. Mukamel, J. Chem. Phys. **109**, 9587 (1998).
[24] A. Guskov, J. Kern, and A. Gabdulkhakov, Nat. Struct. Mol. Biol. **16**, 334 (2009).
[25] N. Kamiya and J.-R. Shen, Proc. Natl. Acad. Sci. U.S.A. **100**, 98 (2003).
[26] G. Raszewski, W. Saenger, and T. Renger, Biophys. J. **88**, 986 (2005).
[27] G. Raszewski, B. A. Diner, E. Schlodder, and T. Renger, Biophys. J. **95**, 105 (2008).
[28] V. Novoderezhkin, J. Dekker, H. van Amerongen, and R. van Grondelle, Biophys. J. **93**, 1293 (2007).
[29] P. F. Tian, D. Keusters, Y. Suzaki, and W. S. Warren, Science **300**, 1553 (2003).
[30] T. Brixner, I. V. Stiopkin, and G. R. Fleming, Opt. Lett. **29**, 884 (2004).
[31] S. Mukamel, Y. Tanimura, and P. Hamm, in *Coherent Multidimensional Optical Spectroscopy*, special issue of Acc. Chem. Res. **42**, 1207 (2009).
[32] See supplementary material at http://dx.doi.org/10.1063/1.3458824 for high-resolution (each 10 fs) evolution of the 2D spectra between $t_2=0$ and 1 ps for CT and QT simulations (check README.TXT file for instructions).
[33] F. Milota, J. Sperling, A. Nemeth, D. Abramavicius, S. Mukamel, and H. F. Kauffmann, J. Chem. Phys. **131**, 054510 (2009).
[34] D. Abramavicius, L. Valkunas, and S. Mukamel, Europhys. Lett. **80**, 17005 (2007).